RSC Advances

PAPER

View Article Online
View Journal | View Issue

Cite this: *RSC Adv.*, 2019, **9**, 7948

Upconversion of transparent glass ceramics containing β-$NaYF_4$:Yb^{3+}, Er^{3+} nanocrystals for optical thermometry

Xinyue Li,*[a] Longyu Yang,[a] Yiwen Zhu,[a] Jiasong Zhong [a] and Daqin Chen *[b]

Received 11th February 2019
Accepted 5th March 2019

DOI: 10.1039/c9ra01088b

rsc.li/rsc-advances

β-$NaYF_4$ nanocrystal embedded glass ceramics were fabricated by a melt-quenching method with subsequent heat-treatment. Structural characterizations and spectrographic techniques were performed to verify the successful precipitation of β-$NaYF_4$ nanocrystals and partition of dopants. Upon excitation of 980 nm, bright green upconversion emission could be achieved in Yb^{3+}, Er^{3+} codoped β-$NaYF_4$ nanocrystal embedded glass ceramics. Furthermore, the temperature-dependent upconversion behaviour based on thermally coupled energy levels was also examined in the range of 300–773 K with the maximum relative sensitivity of 1.24% K^{-1} at 300 K. Accordingly, it has been proved to be a promising candidate for application in optical thermometry.

1. Introduction

Temperature, which is a fundamental parameter, is of unshakeable importance in various fields, covering daily life, science and technology, industrial manufacture and so on.[1–8] In particular, the accuracy of temperature evaluation is urgently crucial. Recently, an ever-increasing focus has been paid to a new type of temperature-measurement technique, which is on the basis of temperature-dependent optical signals, involving luminescence intensity, peak position, full width at half maximum (FWHM) of emission bands, lifetime, fluorescence intensity ratio (FIR) and so on.[9–13] In comparison with traditional temperature measurement methods, this optical thermometry technique possesses unique features such as non-invasiveness, high-resolution, and real time response.

Especially, FIR technique is one of the most promising methods to be applied in practice, owing to its easy operation.[14,15] When two distinguishable emission bands exhibit discrepant temperature behaviour, therefore, the values of their ratio also vary with respect to temperature. Benefit to the evaluation of ratio of two corresponding emission bands, FIR technique can get rid of measuring errors from measurement conditions, for instance fluctuations of excitation source, light scatting and reflection and the drifts of the optoelectronic system. The key factor for FIR technique is identification of two related emission bands. Generally, when the energy gap between two energy levels reaches in the range of 200–2000 cm^{-1}, the signal of emission bands can be separated clearly, getting rid of overlapping of emission bands or losing thermal population from the upper level. As a result, the energy levels that meet this condition are also called the thermally coupled energy levels (TECLs). Coincidentally, lanthanide ions are endowed with enriched energy levels and extremely shaped spectral lines, owing to their 4f–4f transitions. In this way, it would come distinctly that lanthanide ions, for instance Er^{3+}, Ho^{3+}, Dy^{3+} *et al.*, are suitable for FIR-based optical thermometry.[16–20]

But beyond all that, it is quite essential to select suitable host materials. Lanthanide ions doped glass ceramics (GCs) have been honoured as a new class of superior bulk materials, deriving from their favourable integration of low-cost and easy-synthesis of glass and crystal-like optical performance.[21–23] Furthermore, their stable physical and chemical properties have greatly expanded the areas for practical applications. Up to now, oxyfluorides GCs have garnered wide attentions, due to their low phonon energies and high luminescent efficiency.[24–26] Among investigated host materials, β-$NaYF_4$ is a typical example of fluorides.[27,28] It has been recognized as one of the most efficient host materials for upconversion (UC), with the incorporation of Yb^{3+}, Er^{3+} for green UC emission and Yb^{3+}, Tm^{3+} for blue UC emission. In β-$NaYF_4$ crystal lattice, there exists two distinct sites for Y^{3+}. As depicted in Fig. 1(a), half of Y^{3+} is occupied by a fixed site, while the other is randomly occupied with Na^+. Every Y^{3+} is surrounded by nine F^- anions. When lanthanide ions incorporated into the lattice, they prefer to substitute the sites of Y^{3+} consciously. These unique features make β-$NaYF_4$ one of the most efficient host materials for UC.[29,30]

However, it is still not easy to grow β-$NaYF_4$ nanocrystals owing to its cubic-to-hexagonal phase transition during cooling. To our best knowledge, the research on FIR-based optical

[a]*College of Materials & Environmental Engineering, Hangzhou Dianzi University, Hangzhou, 310018, P. R. China. E-mail: lixy@hdu.edu.cn*

[b]*College of Physics and Energy, Fujian Normal University, Fuzhou, 350117, P. R. China. E-mail: dqchen@fjnu.edu.cn*

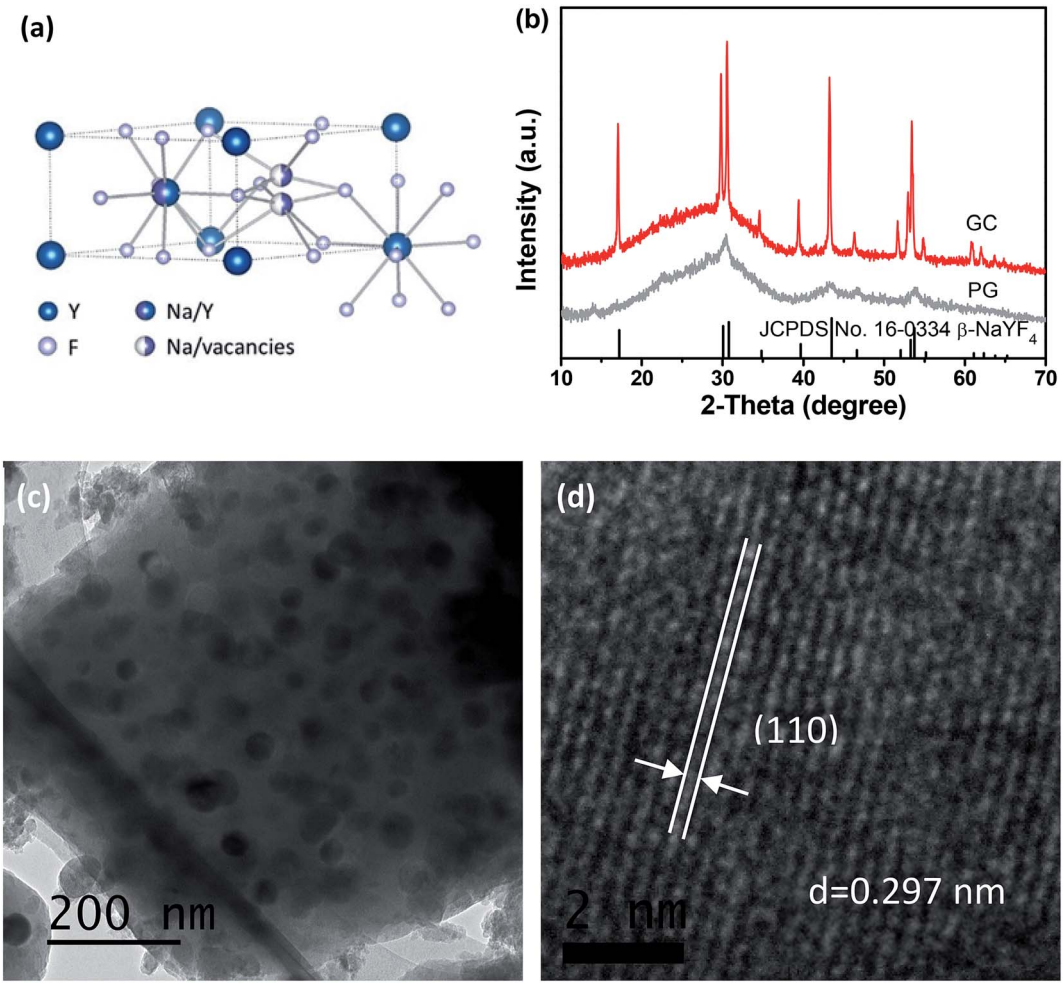

Fig. 1 (a) Crystal structure of β-$NaYF_4$. (b) XRD patterns of PG and GC samples with standard card of β-$NaYF_4$ (JCPDS no. 16–0334). (c) TEM and (d) HRTEM of β-$NaYF_4$ nanocrystal embedded glass ceramics.

thermometry in β-$NaYF_4$ GC has not yet been reported. In our case, self-crystallized β-$NaYF_4$:Yb^{3+}, Er^{3+} nanocrystal embedded GCs were successfully synthesized by traditional melt-quenching method followed by heat-treatment. The precipitation of β-$NaYF_4$ nanocrystals from glass matrix were verified by structural characterizations. Eu^{3+} was incorporated into the β-$NaYF_4$ GC sample to serve as a super-sensitive probe, and the spectrographic feature suggests the partition of dopants. The GC containing β-$NaYF_4$:Yb^{3+}, Er^{3+} nanocrystals exhibited bright UC emission, when excited by 980 nm diode laser. The purpose of this work is to discuss the UC emission properties and mechanism of Yb^{3+}, Er^{3+} codoped β-$NaYF_4$ nanocrystal embedded glass ceramics, and to examine its temperature-dependent behaviour based on FIR technique serving as a candidate for optical thermometry.

2. Experimental section

Traditional melt-quenching method and subsequent heat-treatment was employed to prepare glass ceramics containing β-$NaYF_4$ nanocrystals. Chemical compositions were carefully designed as $55SiO_2$–$10Al_2O_3$–$17Na_2O$–17NaF–$8YF_3$, according to the mechanism for phase-selective growth of $NaYF_4$ reported in our previous studies.[31] All of the raw materials were mixed together and melt at 1450–1550 °C for 30 min, and then poured onto a copper preheated at 300 °C to form precursor glass. In order to release inner stress, the precursor glasses, labelled as PGs, were maintained at 400 °C for 10 h. Glass ceramics, donated as GCs, could be gained after glass crystallization at 650 °C for 2 h.

The crystalline phases of samples were conducted by X-ray diffractometer (Rigaku-TTR-III) with nickel-filtered Cu Kα radiation (λ = 0.15418 nm) in the 2θ range from 10° to 70°. A transmission electron microscopy (TEM, JEM-2010) was employed to characterize the microstructure of GCs. Additionally, scanning transmission electron microscopy (STEM) operated in the high-angle annular dark-field (HAADF) mode was also performed. Furthermore, when excited at 980 nm, the UC emission spectra were recorded by a Jobin-Yvon HRD-1 double monochromator equipped with a Hamamatsu R928 photomultiplier. An Opolette 355 LD laser (410–2200 nm, a spectral line-width of 4–7 cm^{-1}) was chosen as the excitation source for the lifetime measurement. For the measurement of temperature-dependent UC emission spectra, the sample was

loaded on a copper host equipped with a temperature controller (OMRON E5CC-800). The temperature, ranging from 300 K to 773 K, was controlled by a type-K thermocouple and a heating tube.

3. Results and discussion

Fig. 1(b) presents the XRD patterns of PG and GC samples. For the PG, a small quantity of diffraction peaks, assigned to β-$NaYF_4$ (JCPDS no. 16–0334), could be found superimposed on the amorphous hump of glass, suggesting the β-$NaYF_4$ nanocrystals have been already formed in the precursor glass. After heat-treatment, both of the amount and size of β-$NaYF_4$ nanocrystals are increased, so the diffraction peaks of GC are enhanced and sharpened. This crystallization behaviour of glass is call "self-crystallization".[4] Furthermore, morphological features of GC sample were conducted by TEM and high-resolution TEM (HRTEM) images. As exhibited in Fig. 1(c), the β-$NaYF_4$ nanocrystals precipitated homogenously from glass matrix have sized mainly in the range of 30–50 nm. Notably, it can be seen that well-demarcated lattice fringes appear in HRTEM image in Fig. 1(d). The corresponding interplanar spacing *d* is given as 0.297 nm, which matches perfectly with the (110) lattice plane of β-$NaYF_4$. This is a direct evidence for glass crystallization.

Moreover, STEM-HAADF was also performed to examine the element mapping in GC sample. As presented in Fig. 2, elements of Na, Y, F could be found in nanocrystals with introduction of Yb and Er, while Si, Al maintain in the glass matrix. Impressively, Na and F exist in both the nanocrystals and glass. In Fig. 3, EDS spectrum of GC sample also confirms the existence of all above elements. All these results evidence the successful precipitation of β-$NaYF_4$ nanocrystals from aluminosilicate glass and the partition of dopants into β-$NaYF_4$ nanocrystals.

As is well known, Eu^{3+} can serve as a super-sensitive probe to explore the local field it occupies, due to its magnetic dipole transition of $^5D_0 \rightarrow {}^7F_1$ and electric dipole transition of $^5D_0 \rightarrow {}^7F_2$.[32] Therefore, Eu^{3+} is introduced into the GC sample to examine the glass crystallization and partition of dopants, as presented in Fig. 4. Notably, the emission intensities are strongly enhanced after glass crystallization. The ratios of the transitions of $^5D_0 \rightarrow {}^7F_1$ to $^5D_0 \rightarrow {}^7F_2$ are evaluated to be 2.3 for PG and 1.1 for GC, respectively. In addition, the lifetime of Eu^{3+} in GC sample is also lengthened compared to that of PG. Although the PG sample has self-crystallized, the proportion of ordered nanocrystals to disordered glass is still small, remaining residual Eu^{3+} in the glass. After glass crystallization, the percentage of β-$NaYF_4$ nanocrystals has gone up, hence, a majority of Eu^{3+} ions are concentrated in the β-$NaYF_4$ nanocrystals, resulting in an ordered local surrounding. These results provide a compelling evidence for incorporation of dopants into β-$NaYF_4$ nanocrystals.

Under 980 nm laser irradiation, both PG and GC samples exhibit distinct green and red UC emissions of Er^{3+}, which are centred at 520 nm ($^4S_{3/2} \rightarrow {}^4I_{15/2}$), 545 nm ($^2H_{11/2} \rightarrow {}^4I_{15/2}$) and 659 nm ($^4F_{9/2} \rightarrow {}^4I_{15/2}$), respectively. In spite of self-crystallized PG in melt-quenching process, Er^{3+} in the PG sample still exhibit inhomogeneously broadened emissions, which is attributed to small amounts of β-$NaYF_4$ crystals and large amounts of residual dopants in the glass matrix. After glass crystallization, the emission bands of GC are quite enhanced and narrowed, compared to that of PG. Notably, obvious Stark spitting can be also observed for GC sample. All these spectroscopic features indicate that Yb^{3+} and Er^{3+} ions are partitioned into β-$NaYF_4$ nanocrystal embedded glass ceramics. In particular, the green UC emission dominates for GC sample, as evidenced by the inserted photograph in Fig. 5(a), suggesting a huge superiority for TECLs-based optical thermometry of Er^{3+} among various luminescent materials. Furthermore, Fig. 5(b) plots the decay curves of Er^{3+} monitoring at 545 nm and 659 nm. The fitting lifetime of Er^{3+} in GC are demonstrated to be longer than that in PG, which is also a favourable signal for partition of Er^{3+} into β-$NaYF_4$ nanocrystals.

In order to investigate the UC mechanism, the UC emission intensities related to the pump power were measured. It is noteworthy that the relationship between UC emission intensity and the excitation power could be described as the following relation:

$$I \propto P^n \quad (1)$$

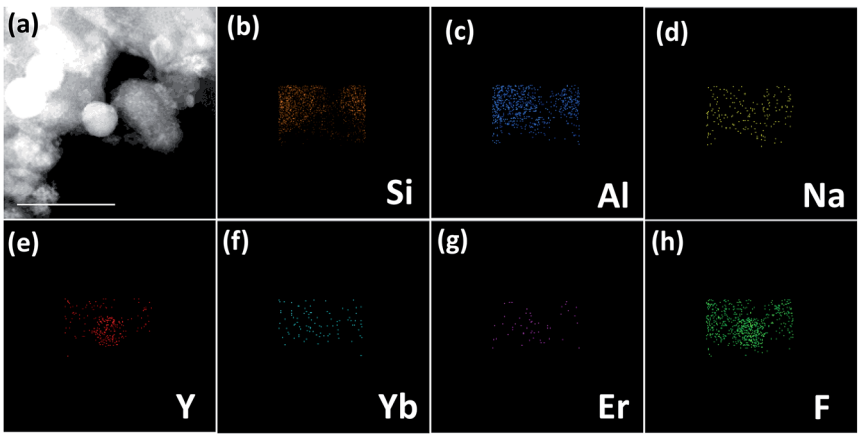

Fig. 2 (a) STEM-HAADF images of GC sample with (b) Si, (c) Al, (d) O, (e) Y, (f) Yb, (g) Er and (h) F elemental mapping.

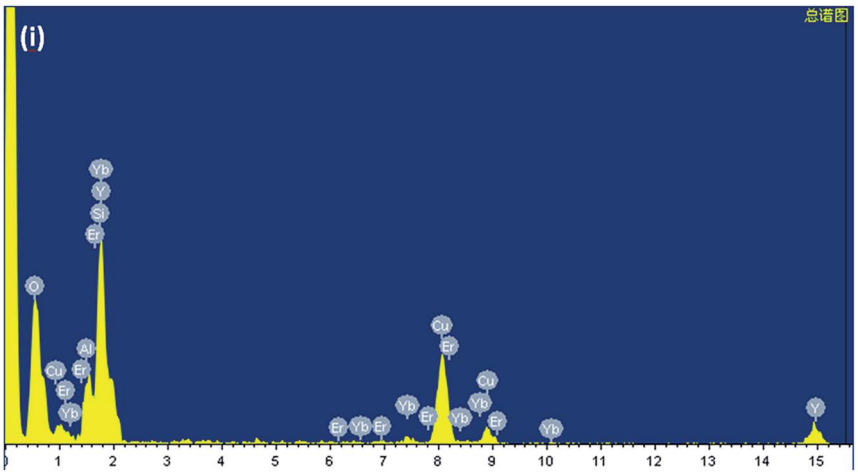

Fig. 3 EDS spectrum of GC sample.

where I is the emission intensity, P is the pump laser power, and n is the number of photons required to populate the upper emitting state. The inset in Fig. 5(a) plots a double logarithmic coordinate, giving n as the slope of the fitting line. When monitoring at 528 nm, 540 nm and 655 nm, the values of n are given as 1.82 ± 0.03, 1.89 ± 0.03 and 1.90 ± 0.04, respectively. These results suggest that both of green and red UC emission are derived from two-photon process.

Fig. 6 illustrates the energy levels diagram of Yb^{3+} and Er^{3+}, as well as possible energy transfer routes for UC. Upon excitation on 980 nm, Yb^{3+} ions act as sensitizers, whose role is to transfer their absorbed energy from excitation source to other activators. In Yb–Er system, Er^{3+} is a typical activator. Two-step energy transfer processes from Yb^{3+} to Er^{3+} occur: $^2F_{5/2} + {}^4I_{15/2} \rightarrow {}^2F_{7/2} + {}^4I_{11/2}$ and $^2F_{5/2} + {}^4I_{11/2} \rightarrow {}^2F_{7/2} + {}^4F_{7/2}$, and then relax to the $^2H_{11/2}$ and $^4S_{3/2}$ emitting states by non-radiative relaxation, producing green UC emission. On the contrary, Er^{3+} populated to $^4I_{11/2}$ state can also relax to the $^4I_{13/2}$ state firstly, and populated to the $^4F_{9/2}$ emitting state through another energy transfer process $^2F_{5/2} + {}^4I_{11/2} \rightarrow {}^2F_{7/2} + {}^4F_{9/2}$, producing red UC emission. It is noteworthy that green and red UC emissions of Er^{3+} originate two-photon process, which is consistent with the power dependence in inset in Fig. 5(a).

As mentioned above, luminescent centre is considerably responsible for its performance as a temperature sensor. For Er^{3+} ions, the dominating UC emission bands centred at 520 nm and 540 nm are assigned to the transitions from the emitting $^2H_{11/2}$ and $^4S_{3/2}$ states, whose energy gap reaches 700–800 cm^{-1} approximately, to the ground $^4I_{15/2}$ state. Undoubtedly, it is quite suitable for TECLs FIR-based optical thermometry. When it works, the relative population of the $^2H_{11/2}$ and $^4S_{3/2}$ energy levels should obey the Boltzmann distribution after reaching a fairly rapid thermal equilibrium, whose ratio corresponds to temperature uniquely. The temperature could be achieved by the ratio. The value of temperature-dependent FIR can be presented as follows:

$$R = B \exp\left(-\frac{\Delta E}{k_B T}\right) \quad (2)$$

where R is the value of FIR, B is a constant, k_B is the Boltzmann constant, ΔE represents the energy gap between the two related TECLs.

As a consequence, the temperature-dependence UC behaviour was investigated systematically in the range of 300–773 K to conduct its FIR-based temperature evaluation performance, as depicted in Fig. 7. Notably, it is of considerably significance to

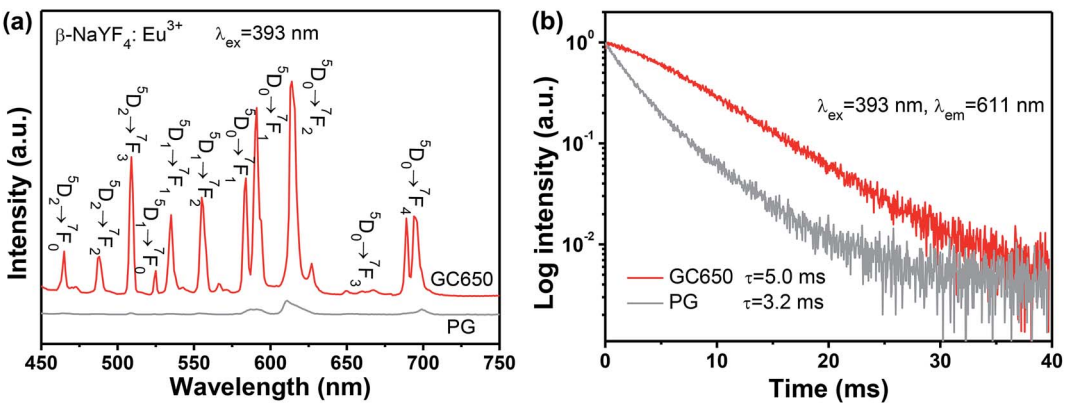

Fig. 4 (a) The emission spectra and (b) the decay curves of GC and PG samples with introduction of Eu^{3+} as a structural probe, under excitation upon 393 nm.

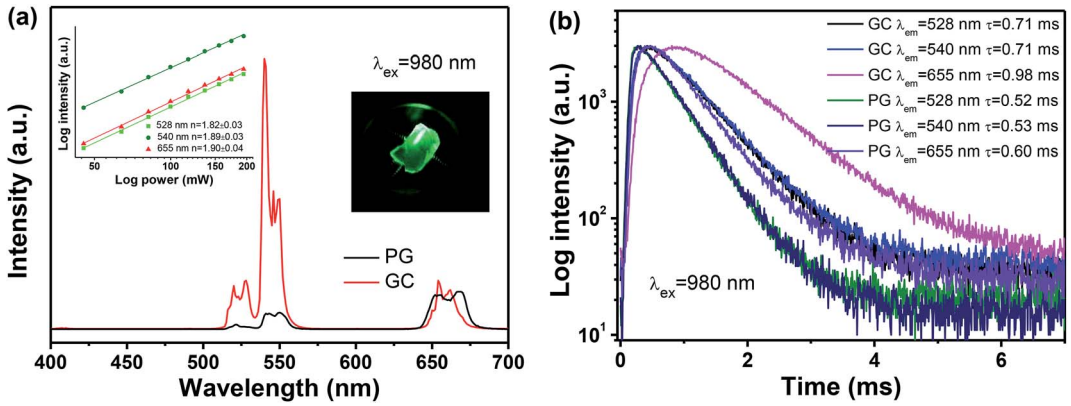

Fig. 5 (a) The UC emission spectra and (b) the decay curves of GC and PG samples containing β-$NaYF_4$:Yb^{3+}, Er^{3+} nanocrystals excited by 980 nm. The inset in (a) illustrates the dependence of UC emission intensities on the pump power of 980 nm. The inserted image is the corresponding luminescence photograph of GC sample under the irradiation of 980 nm.

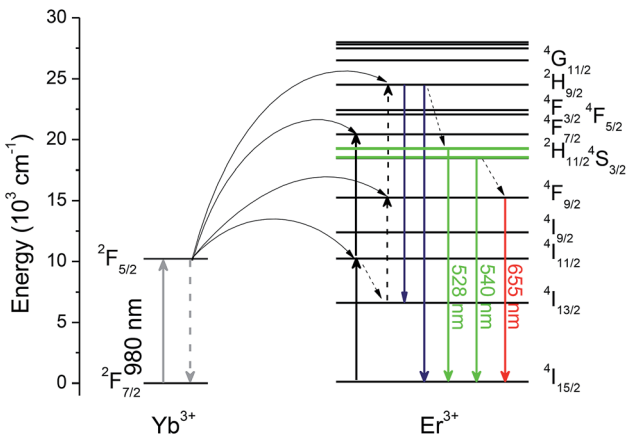

Fig. 6 The diagram of energy levels of Yb^{3+} and Er^{3+}, as well as their possible UC routes.

select suitable pumping power, in order to avoid the heating effect from excitation source. As presented in the inset of Fig. 7(b), the values of FIR were obtained without any obvious fluctuation under different pumping power ranging from 45 mW to 200 mW. In the case of ensuring the good signal-to-noise ratio of the temperature-dependent UC emission spectra, pumping power of 63.9 mW was finally chose as the excitation source for optical thermometry. For clarity, the intensities of the $^4S_{3/2} \rightarrow {}^4I_{15/2}$ transition In Fig. 7(a) are normalized. It can be obviously found that the values of FIR are gradually enhanced, as temperature increasing. Considering its Boltzmann's distributed thermal population, exponential function eqn (1) is employed to fit the experiment data exhibiting the relationship between FIR and temperature. As depicted in Fig. 7(b), the fitting energy gap between the $^4S_{3/2}$ and $^2H_{11/2}$ energy levels could be gained as 773 cm^{-1} during heating process and 770 cm^{-1} during cooling process. Impressively, they are almost the same, suggesting that the value of FIR just depends on temperature rather than measuring processes.

In general, sensitivity S would be employed to evaluate the temperature-dependent performance of a luminescent materials, including the absolute sensitivity S_A and the relative sensitivity S_R. In general, the absolute sensitivity S_A represents the average change in corresponding temperature interval, while the relative sensitivity S_R represents the slope of optical change with temperature. Compared to the absolute sensitivity S_A, the relative sensitivity S_R can be served as a more general form of evaluation on temperature behaviour. In FIR technique, the S_A and S_R could be given as eqn (3) and (4):

$$S_A = \left|\frac{dR}{dT}\right| = R\frac{\Delta E}{k_B T^2} \quad (3)$$

$$S_R = \left|\frac{1}{R}\frac{dR}{dT}\right| = \frac{\Delta E}{k_B T^2} \quad (4)$$

Fig. 7(c) depicts the temperature sensitivities curves, where the blue curve represents the relative sensitivity and the olive-green one represents the absolute sensitivity. Excitedly, the maximum of relative sensitivity is given as 1.24% K^{-1} at 300 K, which is a pretty good result among various FIR-based optical thermometry.[33–36]

As tabulated in Table 1, several typical systems for optical thermometry based TCELs of Er^{3+} were listed. It is not difficult to find that the GC is superior to the glass in terms of the relative sensitivity, owing to its crystal-like local field of Er^{3+}. The narrowed and enhanced emission bands of GC make it more suitable for optical thermometry than glass. Interestingly, temperature evaluation could be achieved excellently in Yb^{3+}–Er^{3+} codoped $NaYF_4$ system, including α-$NaYF_4$ GC,[35] β-$NaYF_4$ GC, β-$NaYF_4$ phosphors[36] or β-$NaYF_4$ nanoparticles.[37] Nevertheless, β-$NaYF_4$ has proved to be more efficient than the α-$NaYF_4$,[31] on the other hand, GC exhibits more stable properties compared to the phosphors and nanoparticles due to its reliable glass network. As a consequence, Yb^{3+}, Er^{3+} codoped β-$NaYF_4$ GC is an outstanding alternative for optical thermometry. Notably, after several cyclic heating and cooling processes, Yb^{3+}, Er^{3+} codoped β-$NaYF_4$ nanocrystal embedded GC exhibit excellent repeatability, which is also a significant indicator for practical application in optical thermometry.

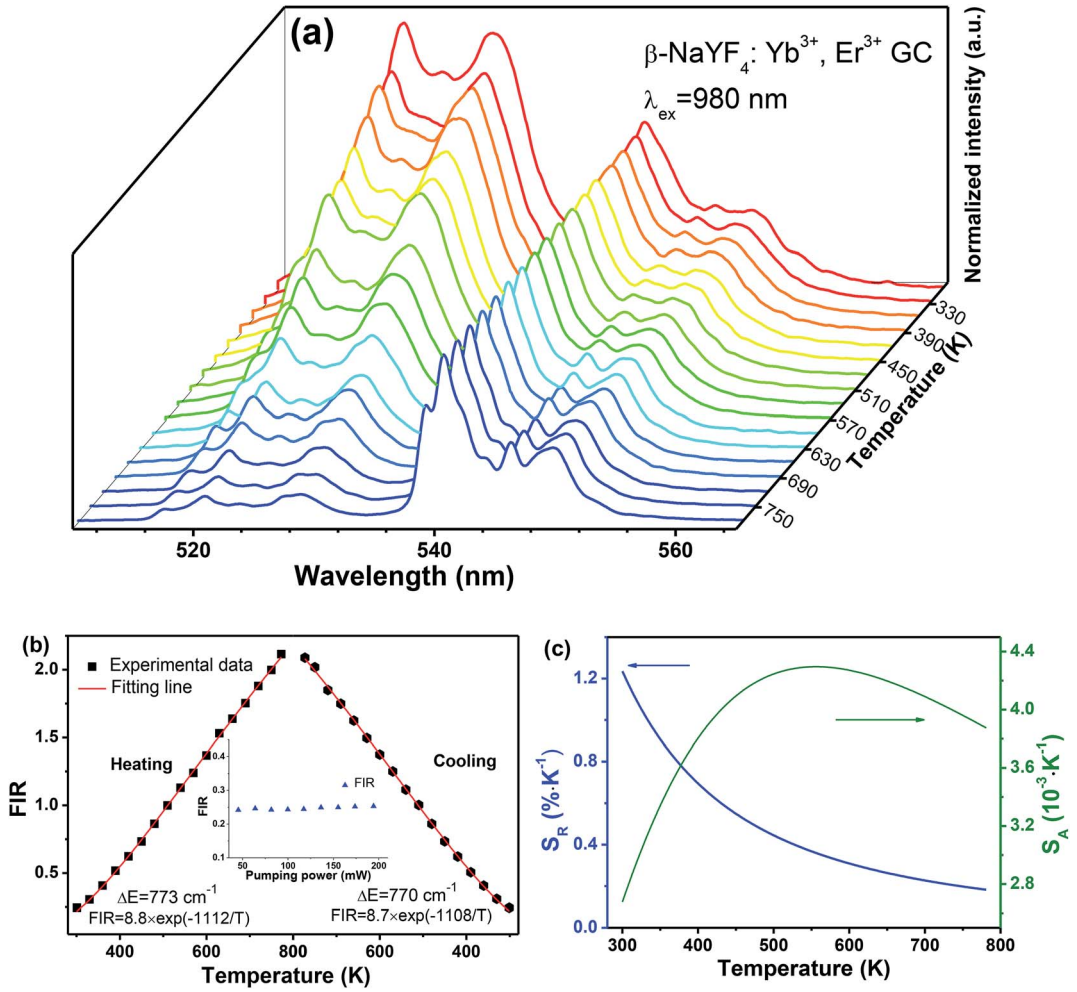

Fig. 7 (a) Normalized UC emission spectra of $NaYF_4$:Er^{3+} GC sample as a function of temperature, and (b) FIR *versus* heating and cooling temperature, and (c) the related sensitivity curves. The inset in (b) represents dependence of FIR on 980 nm laser pumping power.

Table 1 Several related data in Yb–Er systems for optical thermometry

Yb–Er system	Temperature range (K)	Energy gap (cm^{-1})	Relative sensitivity (% K^{-1})	Ref.
TeO_2–WO_3 glasses	300–690	679	977/T^2	33
YF_3–BaF_2–$Ba(PO_3)_2$ glasses	77–500	390	559/T^2	34
α-$NaYF_4$ GC	298–693	775	1117/T^2	35
β-$NaYF_4$ phosphors	160–320	752	1082/T^2	36
β-$NaYF_4$ nanoparticles	299–336	714	1028/T^2	37
β-$NaYF_4$ GC	300–773	773	1112/T^2	This work

4. Conclusion

In summary, hexagonal $NaYF_4$ nanocrystal embedded transparent glass ceramics, which is considered as one of the most optimal host materials for UC, were successfully fabricated *via* melt-quenching method with heat-treatment subsequently. Structural and spectrographic characterizations were performed to indicate the precipitation of β-$NaYF_4$ nanocrystals and partition of dopants from glass matrix. The GC samples exhibit intense UC emission under the excitation of 980 nm, which is favourable for the performance of FIR technique based on the thermal couple levels. The ratio of UC emission originated from the transitions of $^4S_{3/2} \rightarrow {}^4I_{15/2}$ and $^2H_{11/2} \rightarrow {}^4I_{15/2}$ of Er^{3+} exhibited dramatic temperature dependence in the range of 300–773 K, while the maximum relative sensitivity was obtained as 1.24% K^{-1} at 300 K, suggesting that transparent glass ceramics containing β-$NaYF_4$:Yb^{3+}, Er^{3+} nanocrystals offer convincing facts in applications for optical thermometry.

Conflicts of interest

There are no conflicts to declare.

Acknowledgements

This work was financially supported by National Natural Science Foundation of China (51802064 and 51572065), Zhejiang Provincial Natural Science Foundation of China (LY18E020006 and LQ19E020008) and Scientific Research Foundation of Hangzhou Dianzi University (KYS205617012).

References

1 C. D. S. Brites, S. Balabhadra and L. D. Carlos, *Adv. Opt. Mater.*, 2018, **6**, 1701318.
2 X. D. Wang, O. S. Wolfbeis and R. J. Meier, *Chem. Soc. Rev.*, 2013, **42**, 7834–7869.
3 X. F. Wang, Q. Liu, Y. Y. Bu, C. S. Liu, T. Liu and X. H. Yan, *RSC Adv.*, 2015, **5**, 86219–86236.
4 J. S. Zhong, D. Q. Chen, Y. Z. Peng, Y. D. Lu, X. Chen, X. Y. Li and Z. G. Ji, *J. Alloys Compd.*, 2018, **763**, 34–48.
5 L. H. Fischer, G. S. Harms and O. S. Wolfbeis, *Angew. Chem., Int. Ed.*, 2011, **50**, 4546–4551.
6 E. J. McLaurin, V. A. Vlaskin and D. R. Gamelin, *J. Am. Chem. Soc.*, 2011, **133**, 14978–14980.
7 Y. J. Cui, F. L. Zhu, B. L. Chen and G. D. Qian, *Chem. Commun.*, 2015, **51**, 7420–7431.
8 S. S. Zhou, C. K. Duan, M. Yin, X. L. Liu, S. Han, S. B. Zhang and X. M. Li, *Opt. Express*, 2018, **26**, 27339–27345.
9 H. Kusama, J. S. Ojar and Y. Taisuke, *Jpn. J. Appl. Phys.*, 1976, **15**, 2345.
10 X. Y. Li, G. C. Jiang, S. S. Zhou, X. T. Wei, Y. H. Chen, C. K. Duan and M. Yin, *Sens. Actuators, B*, 2014, **202**, 1065–1069.
11 S. S. Zhou, X. Y. Li, X. T. Wei, C. K. Duan and M. Yin, *Sens. Actuators, B*, 2016, **231**, 641–645.
12 B. M. Walsh and B. D. Bartolo, *J. Lumin.*, 2015, **158**, 265–267.
13 W. P. Chen, F. F. Hu, R. F. Wei, Q. G. Zeng and H. Guo, *J. Lumin.*, 2017, **192**, 303–309.
14 L. Li, X. H. Tang, Z. J. Wu, Y. F. Zheng, S. Jiang, X. Tang, G. T. Xiang and X. J. Zhou, *J. Alloys Compd.*, 2019, **780**, 266–275.
15 Y. X. Hao, S. C. Lv, Z. J. Ma and J. R. Qiu, *RSC Adv.*, 2018, **8**, 12165–12172.
16 R. S. Yadav, D. Kumar, A. K. Singh, E. Raia and S. B. Rai, *RSC Adv.*, 2018, **8**, 34699–34711.
17 J. K. Cao, X. M. Li, Z. X. Wang, Y. L. Wei, L. P. Chen and H. Guo, *Sens. Actuators, B*, 2016, **224**, 507–513.
18 X. Y. Li, S. Yuan, F. F. Hu, S. Q. Lu, D. Q. Chen and M. Yin, *Opt. Mater. Express*, 2017, **7**, 3023–3033.
19 Z. M. Cao, S. S. Zhou, G. C. Jiang, Y. H. Chen, C. K. Duan and M. Yin, *Curr. Appl. Phys.*, 2014, **14**, 1067–1071.
20 S. A. Wade, S. F. Collins and G. W. Baxter, *J. Appl. Phys.*, 2003, **94**, 4743–4756.
21 J. B. Zhao, X. L. Zheng, E. P. Schartner, P. Lonescu, R. Zhang, T. Nguyen, D. Y. Jin and H. Ebendorff-Heidepriem, *Adv. Opt. Mater.*, 2016, **4**, 1507–1517.
22 D. Q. Chen, Z. Y. Wan, Y. Zhou, X. Zhou, Y. Yu, J. S. Zhong, M. Y. Ding and Z. G. Ji, *ACS Appl. Mater. Interfaces*, 2015, **7**, 19484–19493.
23 C. G. Lin, C. Bocker and C. Rüssel, *Nano Lett.*, 2015, **15**, 6764–6769.
24 A. Sarakovskis and G. Krieke, *J. Eur. Ceram. Soc.*, 2015, **35**, 3665–3671.
25 D. Q. Chen, Y. Zhou, Z. Y. Wan, H. Yu, H. W. Lu, Z. G. Ji and P. Huang, *Phys. Chem. Chem. Phys.*, 2015, **17**, 7100–7103.
26 A. Herrmann, M. Tylkowski, C. Bocker and C. Rüssel, *Chem. Mater.*, 2013, **25**, 2878–2884.
27 H. X. Mai, Y. W. Zhang, R. Si, Z. G. Yan, L. D. Sun, L. P. You and C. H. Yan, *J. Am. Chem. Soc.*, 2006, **128**, 6426.
28 F. Wang, Y. Han, C. S. Lim, Y. H. Lu, J. Wang, J. Xu, H. Y. Chen, C. Zhang, M. H. Hong and X. G. Liu, *Nature*, 2010, **463**, 1061.
29 S. Fischer, N. D. Bronstein, J. K. Swabeck, E. M. Chan and A. P. Alivisatos, *Nano Lett.*, 2016, **16**, 7241.
30 Y. S. Liu, D. T. Tu, H. M. Zhu, R. F. Li, W. Q. Luo and X. Y. Chen, *Adv. Mater.*, 2010, **22**, 3266.
31 X. Y. Li, D. Q. Chen, F. Huang, G. C. Chang, J. J. Zhao, X. V. Qiao, X. H. Xu, J. C. Du and M. Yin, *Laser Photonics Rev.*, 2018, **12**, 1800030.
32 X. Y. Li, X. Chen, S. Yuan, S. Liu, C. Wang and D. Q. Chen, *J. Mater. Chem. C*, 2017, **5**, 10201–10210.
33 A. Pandey, V. K. Rai, V. Kumar, V. Kumar and H. C. Swart, *Sens. Actuators, B*, 2015, **209**, 352.
34 B. Y. Lai, L. Feng, J. Wang and Q. A. Su, *Opt. Mater.*, 2010, **32**, 1154–1160.
35 S. Jiang, P. Zeng, L. Q. Liao, S. F. Tian, H. Guo, Y. H. Chen, C. K. Duan and M. Yin, *J. Alloys Compd.*, 2014, **617**, 538–541.
36 S. S. Zhou, K. M. Deng, X. T. Wei, G. C. Jiang, C. K. Duan, Y. H. Chen and M. Yin, *Opt. Commun.*, 2013, **291**, 138–142.
37 F. Vetrone, R. Naccache, A. Zamarrón, A. J. de la Fuente, F. Sanz-Rodríguez, L. M. Maestro, E. M. Rodriguez, D. Jaque, J. G. Solé and J. A. Capobianco, *ACS Nano*, 2010, **4**, 3254–3258.